Polymer Chemistry

PAPER

View Article Online
View Journal | View Issue

Cite this: *Polym. Chem.*, 2019, **10**, 5452

Effect of a conjugated/elastic block sequence on the morphology and electronic properties of polythiophene based stretchable block copolymers†

Yun-Chi Chiang,[a] Saburo Kobayashi,[b] Takuya Isono,[b] Chien-Chung Shih,[a] Tomoki Shingu,[b] Chih-Chien Hung,[c] Hui-Ching Hsieh,[a] Shih-Huang Tung,[c,d] Toshifumi Satoh *[b] and Wen-Chang Chen *[a,c,d]

We report the synthesis, morphology, and electronic properties of intrinsically stretchable AB-type, ABA-type, and BAB-type block copolymers (BCPs) of poly(3-hexylthiophene) (P3HT: A block) and elastic poly (octylene oxide) (POO: B block). By incorporating the soft coils, all BCP thin films exhibited clear self-assembled fibrillary nanostructures and largely improved stretchable mechanical properties within the films. The results from the absorption spectra and AFM images indicated that the self-assembled structures of the P3HT blocks in the block copolymers were related to the backbone sequences. Also, the phased-separated morphology of the AB-, ABA-, and BAB-block copolymers from GI-SAXS showed the average nanofibril *d*-spacing ranging from 17.9, 21.6, and 13.9 nm, respectively, which led to the same order on the formed nanofibril density. Among all the BCPs, only the ABA-type BCP thin film remains perfectly smooth and no wrinkle or crack is observed even up to the strain of 100%. These results indicate the significance of the conjugated/elastic block sequence for the morphology and physical properties of the prepared block copolymers. The resistive memory devices fabricated in the configuration of PDMS (substrates)/CNTs (bottom electrode)/BCP thin films (active layer)/Al (top electrode) exhibited non-volatile flash characteristics. In particles, the as-fabricated resistive memory device with the ABA-type BCP could endure up to 80% strain and an excellent ON/OFF current ratio was also achieved after 500 continuous stretching/releasing cycles under 50% strain. This work highlights the importance of molecular architectures on the conjugated/elastic ratios of BCPs for stretchable devices.

Received 13th August 2019,
Accepted 13th September 2019

DOI: 10.1039/c9py01216h

rsc.li/polymers

1. Introduction

In recent years, the rapidly developed flexible or stretchable electronics have drawn extensive research interest owing to their promising potential to be integrated into wearable electronic applications, such as sensors,[1–5] transistors,[6–13] memory devices,[14–17] and other related opto-electronics.[18–20] For example, the electronic skin (E-skin) and smart textiles are vigorously developed to sense, record, and give real-time response to the external environmental stimuli, such as pressure, moisture, temperature, light, *etc*. Therefore, numerous studies have been devoted to developing high-performance materials as well as manufacturing techniques that are suitable for stretchable devices.[21–25]

Among all the basic electronic components, the memory device occupies an important position since all the digital information is stored inside and due to the explosive demand for high data storage density. To meet up with these circumstances, semiconducting polymers with the advantages of structure variability, mechanical flexibility, light-weight, and simple fabrication process are considered as the popular candidates to solve the mechanical problems with human motions. On the other hand, although various types of memory devices have been developed,[26] the most adopted configuration is resistive-type memory devices because of their

[a]*Department of Chemical Engineering, National Taiwan University, Taipei 10617, Taiwan. E-mail: chenwc@ntu.edu.tw*
[b]*Faculty of Engineering and Graduate School of Chemical Sciences and Engineering, Hokkaido University, Sapporo 060-8628, Japan*
[c]*Institute of Polymer Science and Engineering, National Taiwan University, Taipei 10617, Taiwan*
[d]*Advanced Research Center for Green Materials Science and Technology, National Taiwan University, Taipei 10617, Taiwan*

†Electronic supplementary information (ESI) available: Experimental characteristics, ^{1}H-NMR spectrum, SEC traces, and FT-IR spectrum of the studied polymer precursors and block copolymers. TGA and DSC traces, AFM, and GIWAXS images. And additional FET and memory characteristics of the studied polymers. See DOI: 10.1039/c9py01216h

simple architectural structures (a regular diode).[27–30] The working principle of such memory devices is based on their switchable resistance state. That is, the resistance of the active component can be altered by the external electric field. Generally, two different electrically stable states, low- and high-resistance, can be generated and defined as the ON and OFF states. Besides, the memory behaviors of such devices can generally be divided into two categories, namely non-volatile (for example, WORM, write-once-read-many times, and FLASH) and volatile (for example, DRAM, dynamic-random-access-memory, and SRAM, static-random-access-memory) memory behaviors, which possess different features and can be utilized for different applications.[16,31,32]

Benefitting from the good mechanical properties of polymeric materials, the approaches for polymer blends,[33–36] and polymer synthesis,[8,10,37–41] have been widely employed to improve the ductility (*i.e.*, flexibility and stretchability) of the required materials. For example, Bao and co-workers developed a blending system to utilize the nano-confinement effect to reduce the modulus of the conjugated polymer thin films, and thus the as-fabricated devices could be stretched up to 100% strain without affecting the electrical performance.[33] Although the stretchability of the organic semiconductors is improved by the incorporation of elastomers, it is still challenging to develop an intrinsically stretchable material with a high and stable electrical behavior. Hence, the morphology-controllable block copolymer (BCP) consisting of conjugated blocks and insulating elastic blocks is considered to be a promising approach.

As the conjugated segments typically possess strong interchain π–π interactions to facilitate conducting channels, the soft coil blocks can provide the degree of freedom for the polymer chain movement. In our previous studies,[10,15,42,43] we explored linear AB-type BCPs, such as polyfluorene-*block*-poly(pendent isoindigo) (PF-*b*-Piso),[15] poly(3-hexylthiophene)-*block*-poly(*n*-butyl acrylate) (P3HT-*b*-PBA),[10] and polyfluorene-*block*-poly(*n*-butyl acrylate) (PF-*b*-PBA),[42] which were used for stretchable electronic applications. We demonstrated that the introduction of soft coils significantly improved the mechanical resilience, whereas the self-assembled nanofibrillar morphology and the interconnected networks could act as the bearing joints against tensile stress. However, the effect of the conjugated/elastic sequence on the morphology and properties of conjugated block copolymers have not been fully explored yet.

In this study, we report the synthesis, morphology, and properties of conjugated/elastic block copolymers, poly(3-hexylthiophene)-*block*-poly(octylene oxide) (P3HT-*b*-POO)s, with different molecular architectures for the applications of stretchable electronic devices. The studied BCPs, with similar block compositions, were first carefully synthesized according to our previous studies,[10,44] while their architectures were designed to feature different backbone sequences; that is, P3HT-*b*-POO-*b*-P3HT as ABA-type triblock, P3HT-*b*-POO as AB-type diblock, and POO-*b*-P3HT-*b*-POO as BAB-type triblock architectures. The thermal, optical, and mechanical characteristics of these studied materials were explored. The self-assembled nanostructure and thin film morphology upon stretching were investigated using atomic force microscopy (AFM), grazing-incidence small- and wide-angle X-ray scattering (GISAXS/GIWAXS), and optical microscopy (OM) images. In addition, the resistive switching behaviors of the fabricated stretchable devices upon stretching were probed through integrating the studied BCP thin films into the configuration of a polydimethylsiloxane (PDMS)/carbon nanotube (CNT)/BCP film/Al sandwiched structure. We demonstrate that the chain architecture of BCPs plays a crucial role in further improving the mechanical resilience of polymer thin films and maintaining the electronic properties for wearable electronics.

2. Experimental section

2.1 Materials

N,*N*,*N*′,*N*″,*N*″-Pentamethyldiethylenetriamine (PMDETA, 99%), copper(I) bromide (CuBr, 98%), *tert*-butylmagnesium chloride solution (1.0 M in THF), tetrahydrofuran (THF, anhydrous, ≥99.9%), methanol (MeOH, ≥99%), dichloromethane (CH_2Cl_2, anhydrous, ≥99%), *N*,*N*-dimethylformamide (DMF, ≥99%), tetra-*n*-butylammonium fluoride hydrate (TBAF, 98%), 1-*tert*-butyl-4,4,4-tris(dimethylamino)-2,2-bis[tris(dimethylamino)phosphoranylide-namino]-2Λ^5,4Λ^5-catenadi(phosphazene) (*t*-Bu-P_4; 1.0 M solution in *n*-hexane), polydimethylsiloxane (PDMS, Sylgard 184), acetone (≥99.5%), and chloroform ($CHCl_3$, ≥99.9%, stabilized with amylenes) were purchased from Sigma-Aldrich Co. (St Louis, MO). [1,3-Bis(diphenylphosphino)propane]nickel(II) dichloride (Ni(dppp)Cl_2), 1-(3-dimethylaminopropyl)-3-ethylcarbodiimide hydrochloride (EDC), and 4-dimethylaminopyridine (DMAP) were obtained from Tokyo Chemical Industry (TCI). LiCl was purchased from Kanto Chemical Co. (Tokyo, Japan) and dried overnight at 160 °C under high vacuum. Trimethylsilylacetylene (TMSA) was received from Shin-Etsu Chemical Co. (Tokyo, Japan) and purified by distillation over CaH_2 under an argon atmosphere. 2,2-Diethyl-1,3-propanediol (Sigma-Aldrich), 2,5-dibromo-3-hexylthiophene (TCI), 1,2-octylene oxide (TCI), and 3-phenyl-1-propanol (PPA, TCI) were purified by vacuum distillation over CaH_2. Toluene (>99.5%; water content, <0.001%) was purchased from Kanto Chemical, and purified using an MBRAUN solvent purification system. 6-Azidohexanoic acid was prepared according to the previous report. P3HTs and POOs were prepared *via* the Kumada catalyst transfer condensation polymerizations followed by the Sonogashira reaction and the living ring-opening polymerization (ROP), respectively, as reported in our previous studies.[10,44]

2.2 Synthesis

2.2.1 Synthesis of alkynyl-functionalized P3HTs

Synthesis of α-P3HT. In an argon-filled glovebox, anhydrous LiCl (263 mg, 6.19 mmol), 2,5-dibromo-3-hexylthiophene (2.00 g, 6.13 mmol), *t*-BuMgCl (1.0 M in THF; 6.13 mL, 6.13 mmol), and THF (9.20 mL) were sequentially added to a

vial, and the mixture was stirred for 4.5 h at room temperature to prepare the activated Grignard monomer (AGM). The solution was then added to a suspension of Ni(dppp)Cl_2 (108 mg, 204 μmol) and THF (52.13 mL). After stirring for 6 min, the mixture was cooled to −10 °C for 3 min and then a small amount of 5 M HCl was added for another 30 min at the same temperature. The polymer was collected by precipitation in MeOH. The obtained polymer was further purified by washing with MeOH, acetone, and hexane using a Soxhlet apparatus and followed by chloroform extraction and precipitation in MeOH. The as-synthesized polymer was further reacted in a Sonogashira reaction: the polymer (700 mg, 141 μmol), CuBr (40.3 mg, 281 μmol), Pd(PPh_3)$_4$ (162 mg, 141 μmol), and toluene (25.6 mL) were sequentially added into a vial. Under an argon atmosphere, pyridine (8.5 mL) and TMSA (2 mL, 14.06 mmol) were added and stirred at 90 °C for 48 h. The mixture was passed through a neutral Al_2O_3 column and eluted with chloroform to remove the catalyst. The obtained solution was then extracted with 1 N HCl and collected into a flask. After a suitable amount of Na_2SO_4 was added into the solution to remove the residual water, the mixture was then passed through filter paper. Finally, the TMS-protected α-alkynyl-functionalized P3HT (420 mg, 41.2%) was obtained by precipitation in MeOH. $M_{n,NMR}$ = 5500 g mol^{-1}; M_w/M_n = 1.07. ^{1}H NMR (400 MHz, $CDCl_3$, δ (ppm)): 6.97 (s, thiophene), 2.80 (t, J = 5.33 Hz, thiophene–CH_2–), 1.76–1.64 (m, thiophene–CH_2–CH_2–), 1.49–1.23 (m, CH_3–(CH_2)$_3$–), 0.97–0.83 (m, –CH_3), and 0.26 (s, –Si–(CH_3)$_3$).

Synthesis of α,ω-P3HT. In an argon-filled glovebox, anhydrous LiCl (263 mg, 6.19 mmol), 2,5-dibromo-3-hexylthiophene (2.00 g, 6.13 mmol), *t*-BuMgCl (1.0 M in THF; 6.13 mL, 6.13 mmol), and THF (9.20 mL) were sequentially added to a vial, and the mixture was stirred for 4.5 h at room temperature to prepare the activated Grignard monomer (AGM). The monomer solution was then added to a suspension of Ni(dppp)Cl_2 (108 mg, 204 μmol) and THF (52.13 mL). After stirring for 6 min, the mixture was cooled to −10 °C for 3 min. To this reaction mixture, the mixture of TMSA (3.06 mL, 3.06 mmol) and *t*-BuMgCl (1.0 M in THF; 3.06 mL, 3.06 mmol) which had also been stirred for 4.5 h was subsequently added. After stirring for another 30 min at the same temperature, the polymer was collected by precipitation in MeOH. The obtained polymer was further purified by washing with MeOH, acetone, and hexane using a Soxhlet apparatus and followed by chloroform extraction and precipitation in MeOH. The as-synthesized polymer was further reacted in a Sonogashira reaction in the same manner as that mentioned above. Finally, the TMS-protected α,ω-alkynyl-bifunctionalized P3HT (392 mg, 38.4%) was obtained by precipitation in MeOH. $M_{n,NMR}$ = 6350 g mol^{-1}; M_w/M_n = 1.10. ^{1}H NMR (400 MHz, $CDCl_3$, δ (ppm)): 6.97 (s, thiophene), 2.80 (t, J = 5.33 Hz, thiophene–CH_2–), 1.76–1.64 (m, thiophene–CH_2–CH_2–), 1.49–1.23 (m, CH_3–(CH_2)$_3$–), 0.97–0.83 (m, –CH_3), and 0.26 (s, –Si–(CH_3)$_3$).

2.2.2 Synthesis of azido-terminated POOs

Synthesis of mono-functionalized-POO. The synthetic scheme for azido-terminated POO is shown in Scheme 1. The preparation of mono-POO under a typical procedure is as follows: in an argon-filled glovebox, toluene (294 μL), PPA (1.0 M in toluene; 205 μL, 205 μmol), 1,2-octylene oxide (500 mg, 3.90 mmol), and *t*-Bu-P_4 (1.0 M in hexane; 205 μL, 205 μmol) were sequentially added to a vial, and the mixture was stirred at room temperature for 24 h. The polymerization was then quenched by the addition of benzoic acid. The mixture was then dissolved in THF and purified by passing through a pad of neutral Al_2O_3. After the evaporation of solvent, the residue was dried under vacuum to give a high viscosity liquid. The obtained polymer was further reacted in a typical condensation reaction, and dry THF (10 mL), dry DCM (10 mL), the polymer (350 mg, 140 μmol), DMAP (42.8 mg, 350 μmol), EDC (67.1 mg, 350 μmol), and 6-azidohexanoic acid (33.0 mg, 210 μmol) were sequentially added into a flask. The flask was then capped with a $CaCl_2$-filled guard tube and reacted at room temperature for 48 h. The mixture was then evaporated to remove the solvent and reprecipitated in cold MeOH. Finally, mono-POO (470 mg, 89.0%) was obtained after drying under vacuum to give a high viscosity liquid. $M_{n,NMR}$ = 2340 g mol^{-1}, M_w/M_n = 1.07. ^{1}H NMR (400 MHz, $CDCl_3$, δ (ppm)): 7.30–7.12 (m, aromatic), 3.78–3.23 (m, –CH_2CH–polymer backbone–CH_2O–), 2.68 (t, C_6H_5CH_2–), 1.89 (quint, –CH_2C$H_2$$CH_2$–), 1.56–1.19 (m, –OC$H_2$CH(C$H_2CH_2CH_2CH_2CH_2CH_3$)O–), and 0.93–0.80 (m, –OCH_2CH(CH_2CH_2CH_2CH_2CH_2CH_3)O–).

Synthesis of bi-functionalized-POO. In an argon-filled glovebox, toluene (182.6 μL), 2,2-diethyl-1,3-propanediol (1.0 M in toluene; 78 μL, 78 μmol), 1,2-octylene oxide (600 mg, 4.68 mmol), and *t*-Bu-P_4 (1.0 M in hexane; 195 μL, 156 μmol) were sequentially added to a vial, and the mixture was stirred at room temperature for 24 h. The polymerization was quenched by the addition of benzoic acid. The mixture was then dissolved in THF and purified by passing through a pad of neutral Al_2O_3. After the evaporation of solvent, the residue was dried under vacuum to give a high viscosity liquid. The obtained polymer was further reacted in a typical condensation reaction, and dry THF (10 mL), dry DCM (10 mL), the polymer (350 mg, 40 μmol), DMAP (25.2 mg, 210 μmol), EDC (39.5 mg, 210 μmol), and 6-azidohexanoic acid (19.4 mg, 120 μmol) were sequentially added into a flask. The flask was then capped with a $CaCl_2$-filled guard tube and reacted at room temperature for 48 h. The mixture was then evaporated to remove the solvent and reprecipitated in cold MeOH. Finally, bi-POO (412 mg, 78.7%) was obtained after drying under vacuum to give a high viscosity liquid. $M_{n,NMR}$ = 7300 g mol^{-1}, M_w/M_n = 1.03. ^{1}H NMR (400 MHz, $CDCl_3$, δ (ppm)): 3.78–3.23 (m, –CH_2CH–polymer backbone–CH_2O–), 1.56–1.19 (m, –OCH_2CH(CH_2CH_2CH_2CH_2CH_2CH_3)O–), and 0.93–0.80 (m, –OCH_2CH(CH_2CH_2CH_2CH_2CH_2CH_3)O–).

2.2.3 Synthesis of block copolymers with different molecular architectures

Synthesis of AB-type diblock copolymer (P3HT-b-POO). The general procedure for the click reaction is as follows: α-P3HT (110 mg) and CuBr (12.5 mg) were placed in a Schlenk flask, which was evacuated under high vacuum and flushed with argon (three times). On the other hand, mono-POO (128 mg)

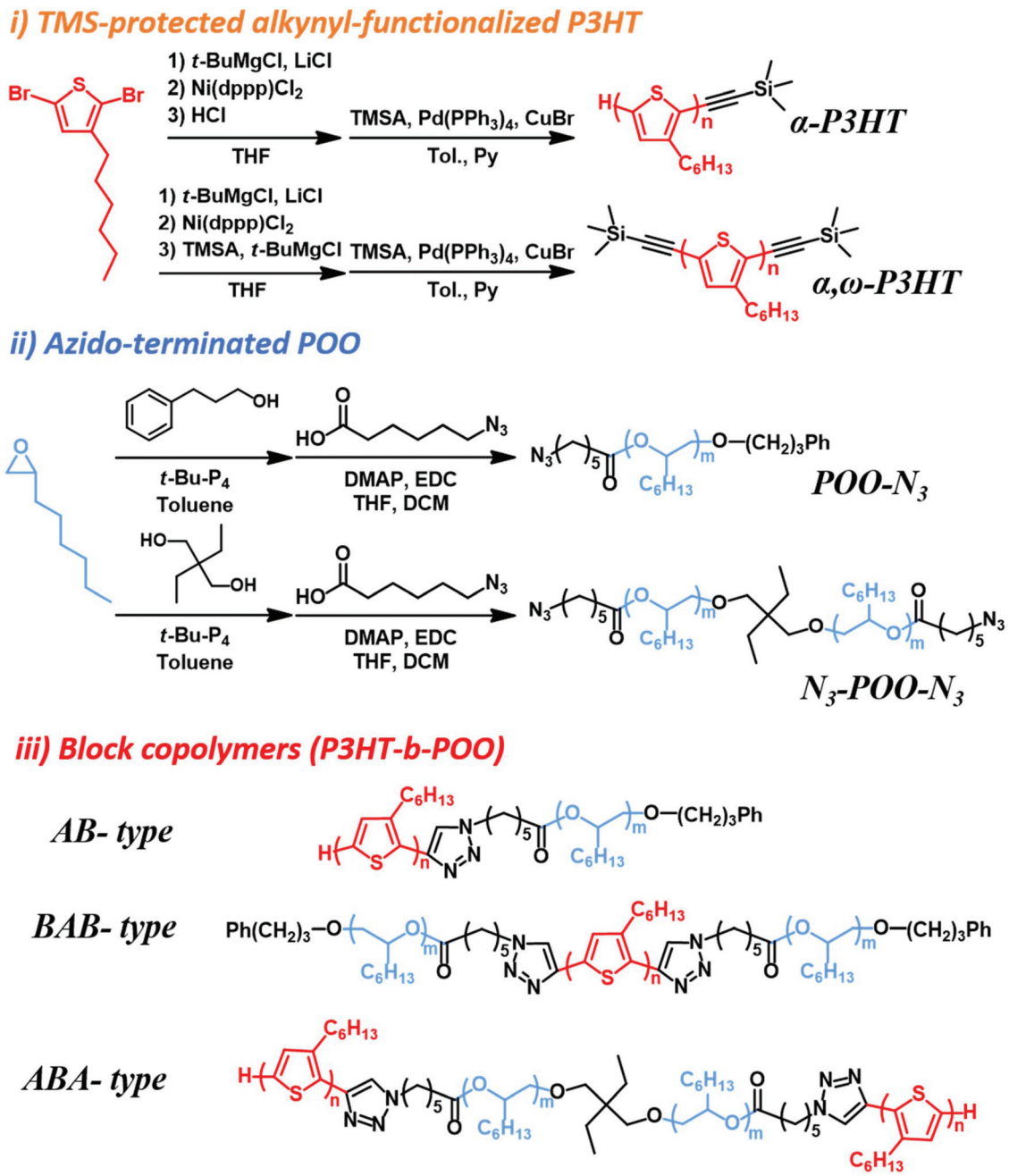

Scheme 1 Synthesis roadmap of AB-type, BAB-type, and ABA-type of studied block copolymers.

and PMDETA (30.1 mg) were prepared in a small amount of dry THF in a vial and degassed by three freeze–pump–thaw cycles. After degassing, the mixture of mono-POO and PMDETA was transferred into the Schlenk flask followed by adding TBAF (1.0 M in THF; 0.1 mL). The sealed mixture was stirred and reacted at 40 °C for 48 h. The SEC traces, ^{1}H NMR and IR were used to check the click reaction. The polymer was purified over a short pad of Al_2O_3 to remove the copper catalyst. After the evaporation of solvent, the residue was precipitated in MeOH. The final product *P3HT-b-POO* was obtained as a dark purple solid (35 mg, 17.9%). $M_{n,NMR}$ = 11 230 g mol^{-1}, M_w/M_n = 1.22. ^{1}H NMR (400 MHz, $CDCl_3$, δ (ppm)): 6.97 (s, H_{ar} P3HT), 3.78–3.23 (m, –CH_2CH–polymer backbone–CH_2O–), 2.80 (t, α–CH_2 P3HT), 1.76–1.64, 1.56–1.19, and 0.97–0.80 (br, alkyl side chains of P3HT and POO).

Synthesis of ABA-type of diblock copolymer (P3HT-b-POO-b-P3HT). As mentioned in the part of *Synthesis of AB-type diblock copolymer (P3HT-b-POO)*, the homopolymers α-P3HT (240 mg) and bi-POO (146 mg) were used for this similar click reaction. The final product *P3HT-b-POO-b-P3HT* was obtained as a dark purple solid (107 mg, 30.2%). $M_{n,NMR}$ = 18 680 g mol^{-1}, M_w/M_n = 1.17. ^{1}H NMR (400 MHz, $CDCl_3$, δ (ppm)): 6.97 (s, H_{ar} P3HT),

3.78–3.23 (m, –CH_2CH–polymer backbone–CH_2O–), 2.80 (t, α–CH_2 P3HT), 1.76–1.64, 1.56–1.19, and 0.97–0.80 (br, alkyl side chains of P3HT and POO).

Synthesis of BAB-type of diblock copolymer (POO-b-P3HT-b-POO). As mentioned in the part of *Synthesis of AB-type of diblock copolymer (P3HT-b-POO)*, the homopolymers α,ω-P3HT (170 mg) and mono-POO (138 mg) were used for this similar click reaction. The final product *POO-b-P3HT-b-POO* was obtained as a dark purple solid (85 mg, 28.8%). $M_{n,NMR}$ = 11 030 g mol^{-1}, M_w/M_n = 1.06. ^{1}H NMR (400 MHz, $CDCl_3$, δ (ppm)): 6.97 (s, H_{ar} P3HT), 3.78–3.23 (m, –CH_2CH–polymer backbone–CH_2O–), 2.80 (t, α–CH_2 P3HT), 1.76–1.64, 1.56–1.19, and 0.97–0.80 (br, alkyl side chains of P3HT and POO).

2.3 Polymer characterization

The ^{1}H NMR (400 MHz) spectra were recorded using a JEOL JNM-ECS400. Size exclusion chromatography (SEC) measurements of the obtained polymers were performed at 40 °C using a Jasco GPC-900 system equipped with two Shodex KF-804L columns (8 mm × 300 mm), where THF was used as the eluent solvent at a flow rate of 1.0 mL min^{-1}. The number-average molecular weight ($M_{n,SEC}$) and polydispersity (M_w/M_n) of the studied polymers were calculated on the basis of polystyrene calibration. The Fourier transform infrared (FT-IR) spectroscopy analysis was carried out using a PerkinElmer Frontier MIR spectrometer equipped with a single reflection diamond universal attenuated total reflection (ATR) accessory. Thermal gravimetric analysis (TGA) was performed using a TA Instruments Q50 at a heating rate of 10 °C min^{-1} from 100 °C to 800 °C under nitrogen flow. Differential scanning calorimetry (DSC) curves of the studied polymers were analyzed *via* a TA Instruments Q100 in which 3–5 mg of samples were heated at a rate of 5 °C min^{-1} from −90 °C to 220 °C.

2.4 Thin film morphology and optical characterization

All the polymer thin films were spin-coated onto an ODTS-modified silicon wafer or cleaned quartz depending on the experimental demand. The polymer solutions were firstly prepared using THF as the processing solvent (concentration of 4 mg mL^{-1}) and heated at 60 °C for at least 2 h to make sure that the solutions dissolved well. Polymer thin films were deposited *via* spin-coating using a rotating speed of 2000 rpm for 60 s. The post-annealing process was carried out at 150 °C under vacuum for 30 min. The nanostructure of polymer thin films was visualized with a Nanoscope 3D controller atomic force micrograph (AFM, Digital Instruments) operating in the tapping mode under an ambient atmosphere. The spring constant of the silicon cantilevers (Nanosensor PPP-SEIHR) was 15 N m^{-1} and the resonant frequency was 330 kHz. Grazing-incident small-angle and wide-angle X-ray scattering (GISAXS/GIWAXS) profiles for the polymer thin films were collected on the beamline BL23A1 and BL13A1 in the National Synchrotron Radiation Research Center (NSRRC, Taiwan). A monochromatic beam of λ = 0.827 Å (15 keV) and λ = 1.02448 Å was used, respectively. The incident angle of both experiments was set as 0.12°. The UV-vis spectra were recorded on a Hitachi U-4100 spectrometer.

2.5 Mechanical properties

Mechanical properties in the thin-film state were probed using an AFM apparatus (Dimension Icon, Bruker) operating in the PeakForce™ tapping mode. The spring constant of the cantilevers with standard silicon tips (OTESPA) is 5–42 N m^{-1} and the force was applied in the range between 5 and 300 nN. Before each measurement, the applied force set point was adjusted to obtain adequate deformation for a reliable fit in the unload region (2 to 10 nm). The tip was set to oscillate at a frequency of 2 kHz, which is far below the cantilever resonant frequency (300 kHz) during the measurement. To determine the elastic moduli of each sample, the collected data were fit with the Derjaguin–Muller–Toporov (DMT) model that is applicable for systems with low adhesion and small tip radii. The reduced modulus E_r is given by

$$F = \frac{4}{3}E_r\sqrt{Rd^3} + F_{adh} = kz$$

where F is the force, R is the tip radius, d is the deformation, F_{adh} is the maximum adhesion force, and z is the vertical displacement.

2.6 Fabrication and characterization of stretchable resistive memory devices

The resistive memory devices were fabricated using a PDMS/CNT/BCP thin film/Al sandwiched structure. The procedure of device fabrication was operated as follows: the CNT-embedded PDMS slabs were firstly prepared as the stretchable electrode and substrate. The polymer thin films, on the other hand, were cast onto an ODTS-modified silicon wafer with 4 mg mL^{-1} polymer solution in THF *via* spin-coating. Subsequently, a post-annealing treatment at 150 °C was carried out under vacuum for 30 min. The polymer thin films were then transferred onto PDMS/CNT slabs through the transfer method. Furthermore, the top electrode (Al, 100 nm) was deposited onto another ODTS-modified silicon wafer using a thermal evaporator at a pressure of 10^{-7} Torr with a depositing rate of 0.5 Å s^{-1}. These top electrodes were again transferred onto PDMS/CNT/BCP thin film slabs *via* the transfer method. During this second transfer process, the top Al electrodes were aligned perpendicular to the bottom CNT patterns, which led to cross-point arrays of memory cells with active joint areas of 0.6 × 1.0 mm^2. The current–voltage characteristics of the devices were measured by using a Keithley 4200-SCS semiconductor parameter analyzer (Keithley Instruments Inc., Cleveland, OH) in a N_2-filled glove box.

3. Results and discussion

3.1 Synthesis and characterization of the block copolymers

As outlined in Scheme 1, the studied BCPs with different architectures: AB-type (P3HT-*b*-POO), BAB-type (POO-*b*-P3HT-*b*-

POO), and ABA-type BCPs (P3HT-*b*-POO-*b*-P3HT), where P3HT is the A block and POO is the B block, were synthesized. The alkynyl-terminated P3HTs were synthesized *via* the Kumada catalyst transfer condensation polymerizations and subsequent end capping with trimethylsilylacetylene (TMS) groups by the Sonogashira reaction, yielding α-functionalized and α,ω-bifunctionalized P3HTs. The ^{1}H NMR spectra are shown in Fig. S1–S3 (ESI†). On the other hand, the azido-functionalized POOs were synthesized through the living anionic ring-opening polymerization (ROP) of 1,2-octylene oxide using 3-phenyl-1-propanol and 2,2-diethyl-1,3-propanediol as the initiator for mono-functionalized and bi-functionalized polymers (POO-OH and HO-POO-OH), respectively. The organic superbase, 1-*tert*-butyl-4,4,4-tris(dimethylamino)-2,2-bis[tris(dimethylamino)-phosphoranylide-namino]-2Λ^5,4Λ^5-catenadi(phosphazene) (*t*-Bu-P$_4$; 1.0 M solution in *n*-hexane), was used as the catalyst while the [monomer]$_0$/[initiator]$_0$ ratios of 19–60 were carefully applied to produce the polymers with desired molecular weights. The obtained POOs were further subjected to a typical condensation reaction with 6-azidohexanoic acid to incorporate the azido end-functional groups, yielding POO-N$_3$ and N$_3$-POO-N$_3$. The ^{1}H NMR spectra of POO-N$_3$ and N$_3$-POO-N$_3$ are shown in Fig. S4–S6 (ESI†). The coupling reaction of the alkynyl-terminated P3HTs and azido-functionalized POOs was carried out by the Cu-catalyzed azido–alkyne click reaction to produce the desired BCPs, *i.e.*, P3HT-*b*-POO, POO-*b*-P3HT-*b*-POO, and P3HT-*b*-POO-*b*-P3HT. A representative ^{1}H NMR spectrum of ABA-type BCP is shown in Fig. 1, which confirms the presence of characteristic protons on both P3HT (peaks a and c) and POO segments (peak b). The corresponding FTIR spectra in the inset of Fig. 1 further exhibits effective coupling between the azido (2100 cm^{-1}) and alkynyl (2140 cm^{-1}) groups before and after the click reaction. The

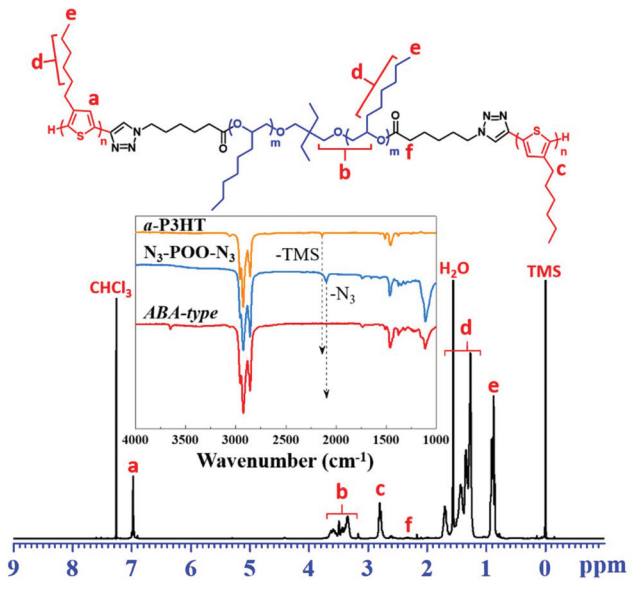

Fig. 1 ^{1}H NMR spectrum of P3HT-*b*-POO-*b*-P3HT and (inset) FTIR spectra of α-P3HT, N$_3$-POO-N$_3$, and P3HT-*b*-POO-*b*-P3HT.

Table 1 Molecular characteristics of the studied block copolymers

	Sample	N_{P3HT} [a]	N_{POO} [a]	$M_{n,SEC}$ [b] (g mol^{-1})	$Đ$ [b]	ω_{P3HT} [a]
ABA	P3HT-*b*-POO-*b*-P3HT	64[c]	56	16 600	1.17	59
AB	P3HT-*b*-POO	37	36	13 800	1.22	56
BAB	POO-*b*-P3HT-*b*-POO	37	32[c]	12 000	1.06	58

[a] Determined by the ^{1}H NMR spectrum. [b] Estimated by SEC in THF using polystyrene as the standard. [c] These numbers are for the sum of the two segments.

corresponding SEC traces of P3HT-*b*-POO-*b*-P3HT (Fig. S7a, ESI†) clearly demonstrate a unimodal peak with an M_w/M_n value of 1.17 and the shift in the elution peak to a higher molecular-weight region in comparison to its precursors, α-P3HT$_{32}$ and N$_3$-POO$_{56}$-N$_3$. Similarly, all the BCPs were completely characterized by ^{1}H NMR, FT-IR and SEC, as shown in Fig. S1–S8 (ESI†). The mass ratios of P3HT in these studied BCPs are carefully controlled within the range of 0.56–0.59 and the corresponding molecular characteristics are listed in Table 1. All the synthesized BCPs are easily soluble in common organic solvents, such as chloroform, dichloromethane, tetrahydrofuran, and toluene.

3.2 Thermal properties

The thermal characteristics of P3HT, POO, and studied BCPs were studied by thermogravimetric analysis (TGA) and differential scanning calorimetry (DSC), as illustrated in Fig. S9 (ESI†) and summarized in Table S1 (ESI†). For pristine P3HT and POO, the thermal decomposition temperatures (T_d, 5% weight-loss) are 413 and 327 °C, respectively. As for the ABA-type, AB-type, and BAB-type BCPs, they all exhibit two distinguished thermal decomposition temperatures that are located between the decomposition temperatures of P3HT and POO blocks. In addition, the overlapped gravimetric traces of the studied BCPs indicate that the mass ratio of P3HT and POO segments is similar. On the other hand, the DSC traces of the studied materials also demonstrate similar thermal behaviors. The glass transition temperature (T_g) and the melting temperature (T_{m1}) of POO blocks within the BCPs are observed in the range of −70 to −66 °C and −17 to −15 °C, respectively, while the T_g and T_{m1} of the pristine POO block are located at −74 °C and −14.6 °C, respectively. Moreover, the melting temperatures (T_{m2}) of P3HT blocks within the BCPs are around 190 °C, whereas the pristine P3HT block shows T_{m2} at 197 °C. Again, the phenomena of similar thermal behavior between ABA-type, AB-type, and BAB-type BCPs are due to the comparable mass ratio of their polymer backbones.

3.3 Physical properties of polymer thin films

Absorption spectroscopy is commonly used to determine the degree of intra- and inter-chain ordering within P3HT polymer chains.[45–47] Fig. 2a shows the normalized solid-state UV-vis spectra of both P3HT and BCP thin films. The spectrum of the pristine P3HT film shows the common absorption peaks at

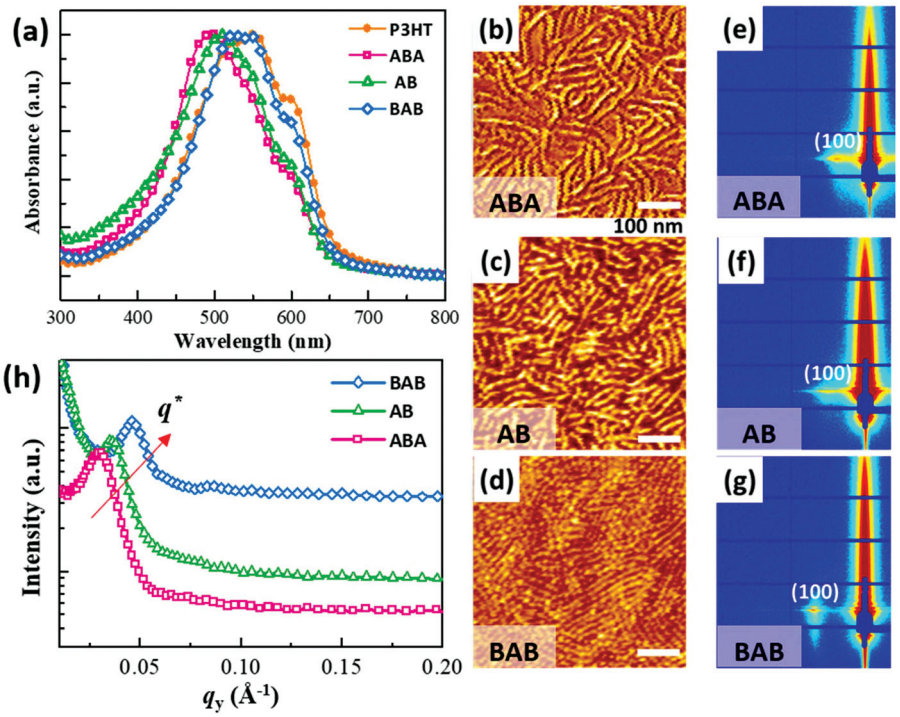

Fig. 2 (a) UV-vis absorption spectra, (b–d) tapping mode AFM phase images, and (e–g) 2-D GISAXS patterns of the annealed thin films. (h) 1-D GISAXS profiles of the studied block copolymers.

520, 555, and 605 nm, indicating the highly regioregular P3HT with an ordered chain configuration and a thermodynamically-preferred planar chain conformation. However, the absorption peaks and the ratio of A_{0-0}/A_{0-1} show shifts for BCPs compared to P3HT, which are probably originating from the difference in polymer assemblies within P3HT blocks. The high energy part of the spectrum is attributed to the disordered chains forming intrachain states. It is most probably related to the chains in the amorphous part of the film, whereas the lower energy part denotes the weakly interacting H-aggregates in the crystalline regions. As we introduced the elastic blocks (*i.e.*, POO) into the polymer chains, the phase-separation nature and the morphology were influenced by the adjacent environment and backbone sequence. Although the maximum absorption peak is markedly blue-shifted, the shoulder of the absorption peak (A_{0-0}) near 605 nm can still be observed in both cases, demonstrating the remaining part of the crystalline region within the thin films. The enthalpies of melting point (T_{m2}) for each polymer are also shown in Table S1 (ESI†). By comparing the enthalpy between pristine P3HT and studied BCPs, all of the BCPs show similar extents of remaining crystallinity from P3HT blocks while BAB-type have a little higher enthalpy which could be attributed to a better crystallinity. That is, if the POO blocks are designed to be linked in the side-position, like BAB-type, the chain conformation along the polymer backbone of P3HT segments adopts a more planar morphology and shares a similar absorption behavior to the pristine P3HT. In contrast, as the P3HT blocks are bonded to the central POO coils, like ABA-type, the absorption peak shows a blue-shift and it indicates weaker intrachain planarization in P3HT aggregates.

Microphase-separated structures of the polymer thin films were investigated by the tapping mode AFM and X-ray diffraction techniques. As shown in Fig. S10 (ESI†), the as-cast (*i.e.*, without thermal annealing) thin films are observed to be featureless for all studied polymers. However, after an annealing process at 150 °C under vacuum for 30 min, all the films turn into a nanofibrillar-like morphology, as shown in Fig. 2b–d and S11 (ESI†). Among the studied BCPs, the ABA-type BCP exhibits the nanostructures that are most loosely distributed, compared to the other BCPs. And the finest nanofibril observed in the BAB-type BCP is most densely distributed. These results indicate that the size and distance between each nanofibril varied with the conjugated/elastic sequence. To gain more insight into the correlation between the morphology and architectures, these thin films were subsequently analyzed using grazing-incidence small-angle X-ray scattering (GISAXS) techniques. As shown in Fig. 2e–h, the 2D patterns and 1D profiles (along the q_y-axis, in-plane direction) of the annealed BCP thin films demonstrate a clear first-order scattering peak at $q^* = 0.291$ nm^{-1} for ABA-, 0.351 nm^{-1} for AB-, and 0.452 nm^{-1} for BAB-type BCPs. The *d*-spacing (*i.e.*, center-to-center distance) is then calculated according to the scattering equation of $d = 2\pi/q^*$, and the corresponding spacing value is determined to be 21.6 nm for ABA-, 17.9 nm for AB-, and 13.9 nm for BAB-type BCPs (Table 2). In addition to the surface structure observed from the AFM images, the GISAXS results further reveal the difference in the distance between

Table 2 Physical properties of annealed polymer thin films

	$\lambda_{maximum}$ [a] (nm)	*d*-Spacing [b] (nm)	Lamellar spacing [b] (nm)	Elastic modulus [c] (MPa)	Crack onset [d] (%)
ABA	498	21.6 ± 0.9	3.86	195	80–100
AB	509	17.9 ± 1.4	3.86	166	40–60
BAB	525	13.9 ± 1.5	3.86	159	20–40

[a] Determined by the UV-vis absorption spectrum. [b] Determined by GISAXS/GIWAXS profiles. [c] Determined by fitting the distribution of elastic modulus. [d] Estimated by OM and AFM images.

each nanofibril within the films, which are driven by the phase separation between the P3HT rods and POO coils. In other words, although the composition of the polymer is nearly the same, the thermodynamically preferred morphology somehow correlates to the molecular architecture and depends on the position of each block.

Fig. 3 schematically shows how the morphology within thin films is influenced by the molecular architectures of the studied BCPs. When the P3HT segments tend to form the crystalline fibrillar structures during annealing, the differences in the chain sequences lead to the varied domains between crystalline and amorphous regions. For example, the POO coils serve as tie chains between P3HTs in the ABA-type, and the outsider P3HTs adopt a more twisted structure and are easier to assemble with other P3HT segments from other polymer chains. As for the BAB-type, the outsider POO coils cause more volumetric hindrance and the insider P3HT segments of polymer chains need to be close enough and aligned to form fibrils. It explains why the absorption peaks shifted. On the other hand, AFM images and GISAXS results also prove the relationship between the spacing and molecular architectures. Since the P3HT segments tend to form the close-packing structure, the position of expelled POO coils is the key to affect the physical and optoelectronic properties.

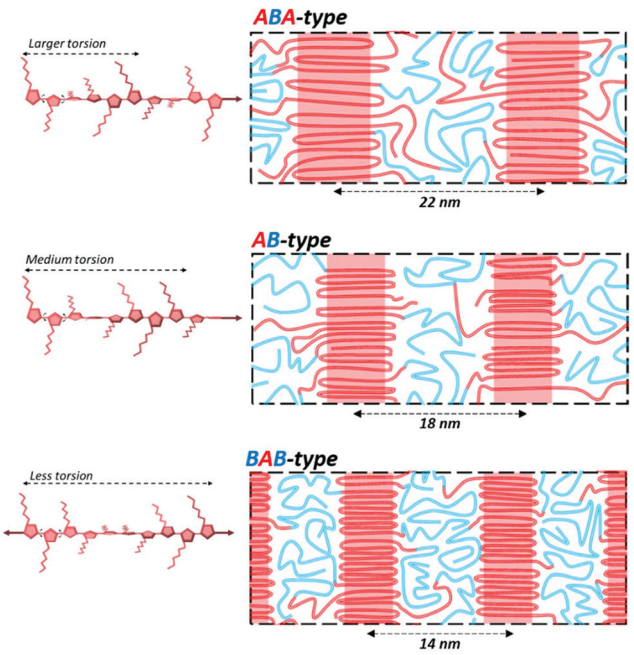

Fig. 3 Schematic illustration of the studied BCPs with different molecular architectures.

The microstructures of the prepared thin films were also investigated *via* the grazing-incidence wide-angle X-ray (GIWAXS) experiment, as shown in Fig. S12 (ESI†). Well-defined edge-on orientation and clear three ordered diffraction peaks can be observed in every BCP. However, the diffraction peaks of BCPs are suppressed because of the incorporation of the elastic POO coils and are thus less crystalline. Since the T_g of POO is around −70 °C, the soft POO coils can not only serve as an insulator matrix but also provide the stretchable characteristics. The PeakForce Quantitative Nanomechanical Mapping (QNM) was further introduced to examine the mechanical properties on the studied films.[48] As shown in Fig. S13 (ESI†), the distribution of the elastic modulus E_s of P3HT and BCPs is extracted by surface mechanical mapping. The averaged elastic modulus of pristine P3HT was 918 MPa, which is similar to the values reported from other measuring techniques.[23,49,50] On the other hand, the averaged elastic moduli of BCPs are in the range of 150 to 200 MPa, which are significantly reduced and close to the values of rubbers (less than 100 MPa). Therefore, the ductility of BCP thin films is clearly improved *via* the incorporation of elastic POO coils.

3.4 Polymer thin films under strains

The practical stretchability of the BCP thin films, namely the crack onset points of films, was examined using optical microscopy (OM). The tested films were prepared by first spin-coating onto an ODTS-modified wafer and subsequently transferred onto the PDMS substrate (15 : 1 mass ratio of base to cross-linker). The strain level was controlled by applying appropriate tensile stress along the PDMS substrates, and the strain-dependent morphology on a micro-scale was thus examined (Fig. 4). Among all the BCPs, only the ABA-type BCP thin film remains perfectly smooth and no wrinkle or crack is observed during the strain. In the case of the AB-type BCP, slight wrinkles appeared upon 40% strain and remained in narrow size as the strain level continuously increased to 100%. After releasing the applied strain, the surface reverts to the original smooth film with nearly no wrinkles. In contrast, as demonstrated in the BAB-type BCP, the wrinkles continuously expand and become irreversible cracks when the strain level increases from 40 to 100%. These cracks remain all over the films even when the stress is released. In addition to the examination on the above micro-scale observation, such stretched films were further explored by AFM. The identical results can be observed in Fig. S14 (ESI†). The distinct nano-scale cracks in a direction perpendicular to the stretching direction firstly appear in the BAB-type BCP, where the strain level is set as 50%. At the same circumstance, the AB-type BCP merely yields some wrinkles within the surface. And these wrinkles become nano-scale cracks as the applied tensile strain was set up to 80%. Unlike the BAB-type and AB-type BCPs, the ABA-type BCP film

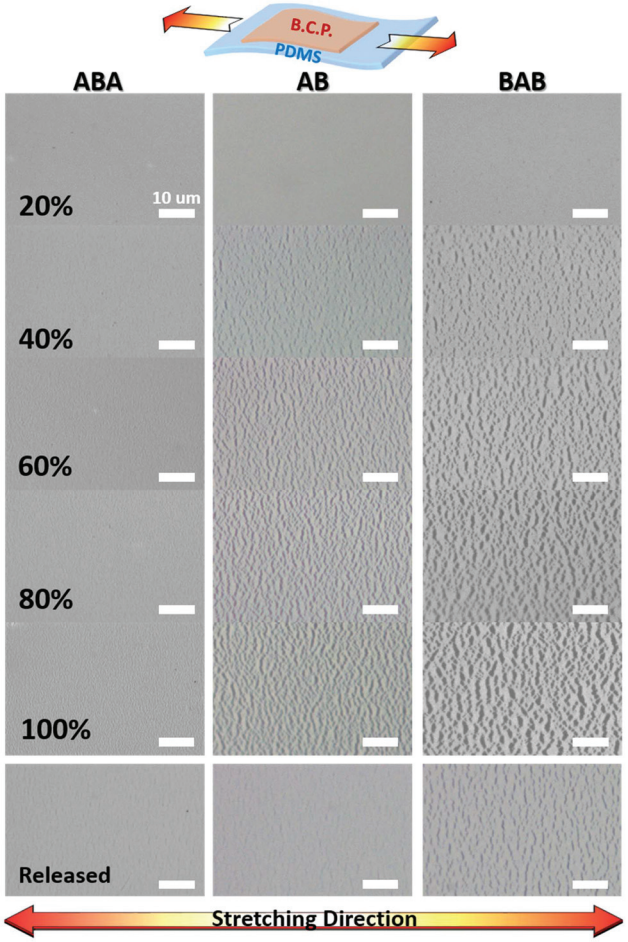

Fig. 4 OM images of the polymer thin films under varying strains.

remains as in the original state and no obvious change is observed under a 50% strain. Furthermore, only wrinkles are observed when the strain elongated up to 80%.

Apart from the direct observation of the ruptures, the stretched films were also elucidated by GISAXS analyses. Two relative directions were applied to the examination of the prepared films and defined as "parallel" and "perpendicular" directions, which represent the orientation between incident X-ray light and the strain direction of films. As presented in Fig. S15 and S16 (ESI†), the *d*-spacing of the nanofibrils within the stretched films shows a strain-dependence behavior only for the ABA-type and AB-type BCPs. As the tensile stress increases along the parallel direction, the first order q values increase, indicating that the distance of each nanofibril reduces due to the compression in the q_y direction (in-plane direction, representing the direction relative to the stretching and the incident X-ray). On the other hand, the q value shifts to the low q region and the spacing is enlarged when the tensile strain increases along the perpendicular direction. As mentioned before, the elastic moduli of BCPs are obviously reduced because of the soft coils, therefore, the mechanical resilience is dramatically improved. However, these could not guarantee the strength of restoration. For example, in the case of the BAB-type BCP, the distance remains almost unchanged during stretching. This is considered as the ruptures took place within the films first, where the tensile stress releases from, rather than elongates or deforms the soft part of polymers. In other words, the ability to enhance the stretchability of polymer thin films is limited and sometimes insignificant even if the elastic coils are introduced. The effective utilization of the hard domains, like some of the crystalline regions can work as the junctions that provide the mechanical strength, becoming a key to further improve the thin film ductility and stretchability. Similar to the widely used elastomeric SBS rubber, poly(styrene-*b*-butadiene-*b*-styrene), the ABA-type BCP possesses the hard segments, namely P3HT blocks, on both sides of each polymer chain. These blocks may self-assemble and join together during the phase-separation process, whereas the middle soft POO blocks then become the extra tie chains to connect the hard domains. To sum up, the hard P3HT domains serve as the physical crosslinking points linked with the soft POO chains, similar to the structure of SBS rubbers, which prevents the films from tearing apart under high strain. And, the ABA-type BCPs are apparently more stretchable than the AB-type and BAB-type BCPs, suggesting the significance of the conjugated rod–coil sequence on the mechanical properties of the prepared block copolymers.

3.5 Electrical characteristics of field-effect transistors and resistive memory devices

The electrical properties of the prepared polymer thin-film transistor and resistive memory devices using the ABA-type, AB-type, and BAB-type BCPs were investigated. FET devices were fabricated with a bottom-gate/top-contact configuration with the ODTS-modified SiO_2 (300 nm, capacitance per unit area = 11.5 nF cm^2) as the gate dielectric layer (Fig. S17a, ESI†). The transfer curves, *i.e.* drain current I_{ds} *vs.* gate voltage V_g, and the corresponding FET electrical characteristics are shown in Fig. S17b (ESI†) and summarized in Table S2 (ESI†). Charge carrier mobilities were calculated from the gate voltage range between −30 and −70 V, where the $I_{ds}^{1/2}$ *vs.* V_g curves showed good linearity. The averaged hole mobilities of the ABA-type, AB-type and BAB-type block copolymer based field-effect transistors are 2.5×10^{-4}, 1.2×10^{-4}, and 7.5×10^{-5} cm^2 V^{-1} s^{-1}, respectively. The difference in the charge carrier mobility between each BCP based OFET device is thought to be attributed to the sizes within the crystalline nanofibrils. The larger and longer nanofibrils offer more appealing charge-transfer mobilities.

On the other hand, the resistive memory devices were fabricated in the configuration of a PDMS (substrate)/CNT (bottom electrode)/BCP thin film (active layer)/Al (top electrode) sandwiched structure, as demonstrated in Fig. 5 and S18 (ESI†). The representative current–voltage (*I*–*V*) characteristics of devices are shown in Fig. 6. The manipulation is detailed as follows: the voltage bias, with a step of 0.05 V, is applied to the top electrode (Al) and the applied voltage is removed right after each voltage sweep. The *I*–*V* curves of the devices are

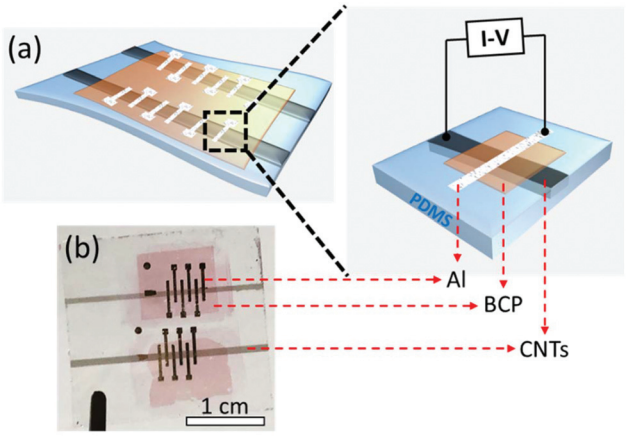

Fig. 5 Schematic illustration of (a) stretchable memory devices and (b) photography of the as-prepared devices.

initially in a high resistance state (that is, OFF state; '0' signal in data storage) with the current in the range of 10^{-9}–10^{-10} A as the voltage swept from 0 to around 1.8 V. Subsequently, the current switches from a high resistance state to a low resistance state (that is, ON state; '1' signal in data storage) with a threshold voltage of approximately 1.8 V. It should be noted that this electronic transition from the OFF state to the ON state during the voltage sweep serves as the writing process. After that, the device stored the information and remained in the ON state as another voltage sweep is applied (sweep 2), showing the bistable states with an ON/OFF current ratio up to 10^5 when the current was read at 0.5 V. After that, a third sweep using the same memory cell with a negative voltage bias was applied. In the early stage of this third sweep, the current initially remained in low resistance until a sudden drop occurred. The second electronic transition from the ON state to the OFF state appears during this negative voltage sweep, which is the erasing process. Right after the third sweep, the memory returns into the high resistance state, OFF state, and forgets the previous information, indicating the non-volatile FLASH memory behavior.

Interestingly, all BCPs not only demonstrate the FLASH behaviors but also exhibit a similar electrical performance. No matter which BCP is used as the active layer, all the memory cells can turn into a low-resistance ON state *via* a positive voltage bias, and return back into a high-resistance OFF state by applying a negative bias. Table 3 lists the electrical characteristics of the as-fabricated resistive memory devices. The averaged threshold voltages during the writing and erasing processes are summarized from at least 20 memory cells and

Table 3 Electrical characteristics of the resistive memory devices

			$V_{threshold}$ [a]	
Code	Memory type	On/off ratio[a]	Writing	Erasing
ABA	Flash	10^4–10^5	1.86 ± 0.27	−1.81 ± 0.58
AB	Flash	10^4–10^5	1.73 ± 0.16	−2.16 ± 0.61
BAB	Flash	10^4–10^5	1.77 ± 0.19	−1.90 ± 0.43

[a] The electrical properties are averaged from at least 20 memory cells of 3 batches.

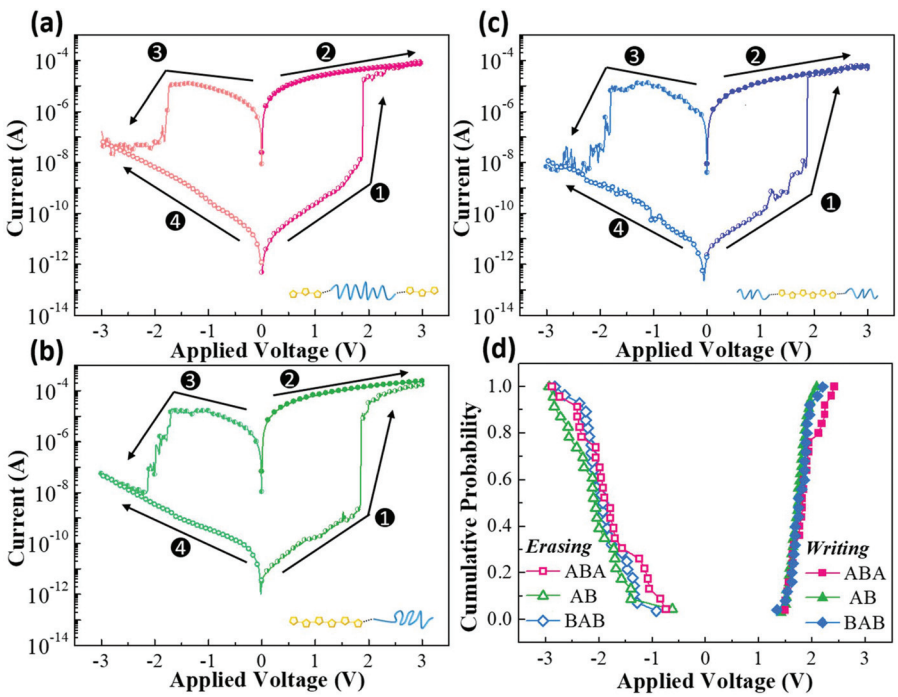

Fig. 6 *I*–*V* characteristics of the resistive memory devices. (a) ABA-type, (b) AB-type, and (c) BAB-type. (d) Cumulative probability of SET/RESET threshold voltages.

the corresponding cumulative probability is depicted in Fig. 6d, demonstrating an insignificant difference between each batch of device fabrications and high performance stability. By comparing with our previous reports and the above-mentioned results,[15,51] it suggests that the electrical properties strongly depend on the P3HT/POO ratio, while the sequence of each block is more significant to the mechanical properties rather than electrical characteristics.

Additionally, the fabricated memory devices were further examined by the repeating programming/deprogramming test, namely the write–read–erase–read (W–R–E–R) cycles, as shown in Fig. S19 (ESI†). The W–E–R–E cycles are performed under a preprogramed voltage sequence: (1) 3 V as the writing process; (2) 0.5 V to read the electrical bistable state, ON state in this time; (3) −3 V as the erasing process; and again (4) 0.5 V to read the electrical bistable state, OFF state. All the studied BCPs show a reprogrammable performance with the ON/OFF ratio up to 10^4. On the other hand, the long-term stability with the stable ON and OFF states can be maintained for at least 10^4 s under a voltage bias of 0.5 V and exhibit a high ON/OFF ratio of around 10^5. It demonstrates that the studied materials used as the active layer in resistive memory devices have stable resistive switching characteristics. Thus, high-performance resistive memory devices with excellent FLASH behavior are achieved.

3.6 Stretchable resistive memory devices

To make the device stretchable, we slightly change the fabrication process described in Fig. S18 (ESI†). The Al top electrodes are, on the other hand, transferred onto the pre-strained PDMS/CNT/thin film half-device for stretchability. The memory characteristics of such devices using the studied BCPs as the active layer under varying tensile strains, from 0 to 80%, are then examined. The *I–V* characteristics of the devices using different types of BCPs under 25%, 50% and 80% strains are shown in Fig. 7. When the devices are applied under 25% strain, the well-defined FLASH electrical responses could still be observed for all the ABA-type, AB-type, and BAB-type BCP devices, which have the ON/OFF memory ratio of up to 10^5 at 0.5 V. It suggests that the stretchable electronic devices are successfully achieved. However, as the applied strain increases up to 50%, the OFF state current increases apparently for the BAB-type BCP devices and the corresponding ON/OFF ratio only remains the order of 10. As for the ABA-type and AB-type BCP devices, they exhibit good performance although slight shifts in threshold voltages are observed. This may be attributed to the fractures yielded in the BAB-type thin films that result in easy penetration of the electricity within the active layer, however, the films of ABA-type and AB-type BCPs just become thinner. The same condition happened to the AB-type BCP devices when the applied strain increases up to the 80% strain. On the other hand, ABA-type BCP devices maintain excellent electrical response even under 80% strain. The strained ABA-type BCP devices also performed well in the W–R–E–R cycles and retention times, as shown in Fig. S20 (ESI†). Stable reprogrammable performance with the ON/OFF ratio up to 10^4 for 100 programming cycles, and long-term stability with steady ON and OFF states up to 10^4 s are accomplished. These electrical behaviors under varying strain levels are thus agreeing with the above-mentioned results demonstrated *via* OM and AFM images.

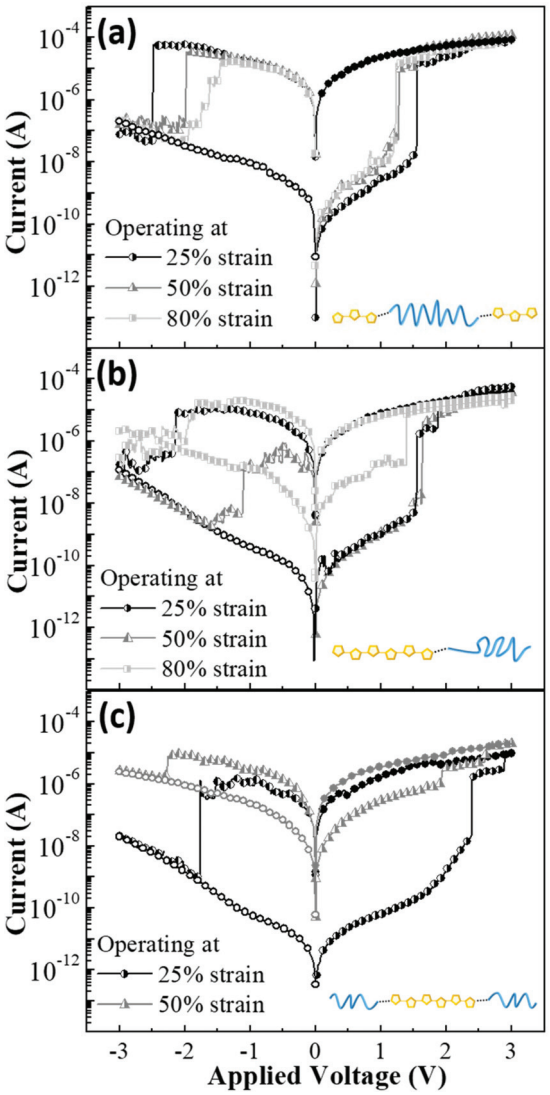

Fig. 7 *I–V* characteristics of the stretchable devices under varying strains. (a) ABA-type, (b) AB-type, and (c) BAB-type.

Nevertheless, the ABA-type BCP devices were also examined with repeated stretching/releasing cycle tests to determine the mechanical stability, as 500 cycles of continuous stretch-relaxation tensile stress under 50% strain were carried out (Fig. 8). The *I–V* characteristics of the devices after varying stretching cycles are shown in Fig. 8a. The ON/OFF current ratio, at the reading voltage of 0.5 V, and the threshold voltages, including the writing and erasing process, are summarized in Fig. 8b. Although the threshold voltages for the writing and erasing process are shifted slightly, the well-defined electrical characteristics of the FLASH type memory are maintained. The ON/OFF current ratio is reduced after the cycling test, which is

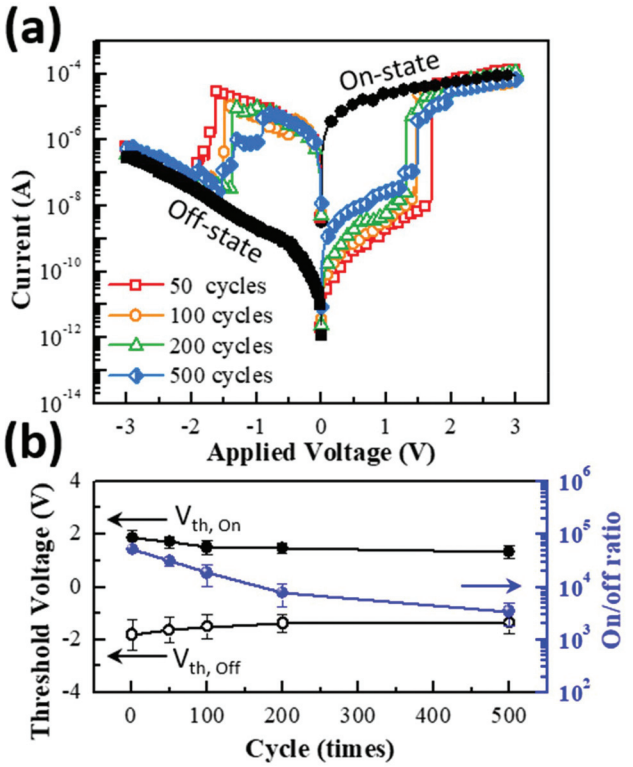

Fig. 8 (a) *I–V* characteristics and (b) mechanical endurance of P3HT-*b*-POO-*b*-P3HT-based stretchable devices under 50% strain for 1–500 stretch/release cycles.

probably due to the doping phenomena under ambient conditions. However, it is still higher the order of 10^3 after 500 cycles. The corresponding W–R–E–R cycles and long-term stability retention times are also shown in Fig. S21 (ESI†), with the endurance of the W–R–E–R cycles, after 500 cycles of 50% strain, shown in Fig. S22 (ESI†). Apart from the electrical performance, the AFM images of these films further confirm the mechanical stability of the ABA-type BCP during the vigorously repeated strain cycles (Fig. S23, ESI†). The above-mentioned results provide the importance of architecture design to use BCPs as the stretchable active layers and demonstrate the excellent stretchability with stable electrical performance of our stretchable resistive memory devices.

4. Conclusions

We have systematically investigated the conjugated/elastic block sequence of poly(3-hexylthiophene)-*block*-poly(octylene oxide) BCPs. The experimental results revealed the significance of the conjugated/elastic sequence for morphologies, mechanical properties and the as-prepared stretchable device characteristics. On comparing the AFM images and GISAXS analyses, the differences in the self-assemblies of the P3HT blocks and the average nanofibril *d*-spacing range showed a relationship with their architectures (ABA > AB > BAB). Among all the BCPs, only the ABA-type BCP thin film remains perfectly smooth and no wrinkle or crack is observed even up to the strain of 80%, indicating the significance of the conjugated/elastic sequence and a more suitable structure of ABA-type for intrinsically stretchable BCP. The as-fabricated resistive memory device in the configuration of PDMS/CNTs/BCP thin films/Al with the ABA-type BCP showed non-volatile flash memory characteristics and could endure 500 continuous stretching/releasing cycles under 50% strain. This work highlights the importance of the molecular architectures on the conjugated/elastic BCPs for stretchable devices.

Conflicts of interest

The authors declare no conflicts of interest.

Acknowledgements

The authors appreciate the financial support by the "Advanced Research Center for Green Materials Science and Technology" from the Featured Area Research Center Program within the framework of the Higher Education Sprout Project by the Ministry of Education (108L9006) and the Ministry of Science and Technology in Taiwan (MOST 108-3017-F-002-002). The authors also acknowledge the National Synchrotron Radiation Research Center of Taiwan for facilitating the GIXD experiments.

References

1 Q. Hua, J. Sun, H. Liu, R. Bao, R. Yu, J. Zhai, C. Pan and Z. L. Wang, *Nat. Commun.*, 2018, **9**, 244.
2 S. Zhao, J. Li, D. Cao, G. Zhang, J. Li, K. Li, Y. Yang, W. Wang, Y. Jin, R. Sun and C.-P. Wong, *ACS Appl. Mater. Interfaces*, 2017, **9**, 12147–12164.
3 J. Tolvanen, J. Hannu and H. Jantunen, *Sci. Rep.*, 2018, **8**, 13241.
4 H. Souri and D. Bhattacharyya, *ACS Appl. Mater. Interfaces*, 2018, **10**, 20845–20853.
5 Z. Tang, S. Jia, F. Wang, C. Bian, Y. Chen, Y. Wang and B. Li, *ACS Appl. Mater. Interfaces*, 2018, **10**, 6624–6635.
6 J. Y. Oh, S. Rondeau-Gagné, Y.-C. Chiu, A. Chortos, F. Lissel, G.-J. N. Wang, B. C. Schroeder, T. Kurosawa, J. Lopez, T. Katsumata, J. Xu, C. Zhu, X. Gu, W.-G. Bae, Y. Kim, L. Jin, J. W. Chung, J. B. H. Tok and Z. Bao, *Nature*, 2016, **539**, 411.
7 Y.-L. Rao, A. Chortos, R. Pfattner, F. Lissel, Y.-C. Chiu, V. Feig, J. Xu, T. Kurosawa, X. Gu, C. Wang, M. He, J. W. Chung and Z. Bao, *J. Am. Chem. Soc.*, 2016, **138**, 6020–6027.
8 J. Mun, G. J. N. Wang, J. Y. Oh, T. Katsumata, F. L. Lee, J. Kang, H. C. Wu, F. Lissel, S. Rondeau-Gagné, J. B. H. Tok and Z. Bao, *Adv. Funct. Mater.*, 2018, **28**, 1804222.
9 H.-C. Wu, C.-C. Hung, C.-W. Hong, H.-S. Sun, J.-T. Wang, G. Yamashita, T. Higashihara and W.-C. Chen, *Macromolecules*, 2016, **49**, 8540–8548.

10 J.-T. Wang, S. Takshima, H.-C. Wu, C.-C. Shih, T. Isono, T. Kakuchi, T. Satoh and W.-C. Chen, *Macromolecules*, 2017, **50**, 1442–1452.
11 Y. Li, W. K. Tatum, J. W. Onorato, Y. Zhang and C. K. Luscombe, *Macromolecules*, 2018, **51**, 6352–6358.
12 S. Y. Son, J.-H. Kim, E. Song, K. Choi, J. Lee, K. Cho, T.-S. Kim and T. Park, *Macromolecules*, 2018, **51**, 2572–2579.
13 Y. Lee, M. Shin, K. Thiyagarajan and U. Jeong, *Macromolecules*, 2016, **49**, 433–444.
14 Y. Sun, X. Zheng, X. Yan, Q. Liao, S. Liu, G. Zhang, Y. Li and Y. Zhang, *ACS Appl. Mater. Interfaces*, 2017, **9**, 43822–43829.
15 J.-T. Wang, K. Saito, H.-C. Wu, H.-S. Sun, C.-C. Hung, Y. Chen, T. Isono, T. Kakuchi, T. Satoh and W.-C. Chen, *NPG Asia Mater.*, 2016, **8**, e298.
16 C. C. Hung, Y. C. Chiu, H. C. Wu, C. Lu, C. Bouilhac, I. Otsuka, S. Halila, R. Borsali, S. H. Tung and W. C. Chen, *Adv. Funct. Mater.*, 2017, **27**, 1606161.
17 L.-C. Hsu, C.-C. Shih, H.-C. Hsieh, Y.-C. Chiang, P.-H. Wu, C.-C. Chueh and W.-C. Chen, *Polym. Chem.*, 2018, **9**, 5145–5154.
18 J. Liang, L. Li, X. Niu, Z. Yu and Q. Pei, *Nat. Photonics*, 2013, **7**, 817.
19 M. Vosgueritchian, J. B. H. Tok and Z. Bao, *Nat. Photonics*, 2013, **7**, 769.
20 L. Li, J. Liang, H. Gao, Y. Li, X. Niu, X. Zhu, Y. Xiong and Q. Pei, *ACS Appl. Mater. Interfaces*, 2017, **9**, 40523–40532.
21 S. Wang, J. Xu, W. Wang, G.-J. N. Wang, R. Rastak, F. Molina-Lopez, J. W. Chung, S. Niu, V. R. Feig, J. Lopez, T. Lei, S.-K. Kwon, Y. Kim, A. M. Foudeh, A. Ehrlich, A. Gasperini, Y. Yun, B. Murmann, J. B. H. Tok and Z. Bao, *Nature*, 2018, **555**, 83.
22 Y. Liu, Z. Liu, B. Zhu, J. Yu, K. He, W. R. Leow, M. Wang, B. K. Chandran, D. Qi, H. Wang, G. Chen, C. Xu and X. Chen, *Adv. Mater.*, 2017, **29**, 1701780.
23 A. D. Printz and D. J. Lipomi, *Appl. Phys. Rev.*, 2016, **3**, 021302.
24 Y. Qian, X. Zhang, L. Xie, D. Qi, B. K. Chandran, X. Chen and W. Huang, *Adv. Mater.*, 2016, **28**, 9243–9265.
25 B. Kang, E. Song, S. B. Lee, B.-G. Chae, H. Ahn and K. Cho, *Chem. Mater.*, 2018, **30**, 6353–6360.
26 P. Heremans, G. H. Gelinck, R. Müller, K.-J. Baeg, D.-Y. Kim and Y.-Y. Noh, *Chem. Mater.*, 2011, **23**, 341–358.
27 S. Song, B. Cho, T. W. Kim, Y. Ji, M. Jo, G. Wang, M. Choe, Y. H. Kahng, H. Hwang and T. Lee, *Adv. Mater.*, 2010, **22**, 5048–5052.
28 W. P. Lin, S. J. Liu, T. Gong, Q. Zhao and W. Huang, *Adv. Mater.*, 2014, **26**, 570–606.
29 H. Ling, M. Yi, M. Nagai, L. Xie, L. Wang, B. Hu and W. Huang, *Adv. Mater.*, 2017, **29**, 1701333.
30 W.-J. Joo, T.-L. Choi, J. Lee, S. K. Lee, M.-S. Jung, N. Kim and J. M. Kim, *J. Phys. Chem. B*, 2006, **110**, 23812–23816.
31 L.-H. Xie, Q.-D. Ling, X.-Y. Hou and W. Huang, *J. Am. Chem. Soc.*, 2008, **130**, 2120–2121.
32 H.-C. Wu, C.-L. Liu and W.-C. Chen, *Polym. Chem.*, 2013, **4**, 5261–5269.
33 J. Xu, S. Wang, G.-J. N. Wang, C. Zhu, S. Luo, L. Jin, X. Gu, S. Chen, V. R. Feig, J. W. F. To, S. Rondeau-Gagné, J. Park, B. C. Schroeder, C. Lu, J. Y. Oh, Y. Wang, Y.-H. Kim, H. Yan, R. Sinclair, D. Zhou, G. Xue, B. Murmann, C. Linder, W. Cai, J. B.-H. Tok, J. W. Chung and Z. Bao, *Science*, 2017, **355**, 59–64.
34 B. Kang, F. Ge, L. Qiu and K. Cho, *Adv. Electron. Mater.*, 2017, **3**, 1600240.
35 H. J. Kim, M. Y. Lee, J.-S. Kim, J.-H. Kim, H. Yu, H. Yun, K. Liao, T.-S. Kim, J. H. Oh and B. J. Kim, *ACS Appl. Mater. Interfaces*, 2017, **9**, 14120–14128.
36 G. Zhang, M. McBride, N. Persson, S. Lee, T. J. Dunn, M. F. Toney, Z. Yuan, Y.-H. Kwon, P.-H. Chu, B. Risteen and E. Reichmanis, *Chem. Mater.*, 2017, **29**, 7645–7652.
37 H.-F. Wen, H.-C. Wu, J. Aimi, C.-C. Hung, Y.-C. Chiang, C.-C. Kuo and W.-C. Chen, *Macromolecules*, 2017, **50**, 4982–4992.
38 R. Peng, B. Pang, D. Hu, M. Chen, G. Zhang, X. Wang, H. Lu, K. Cho and L. Qiu, *J. Mater. Chem. C*, 2015, **3**, 3599–3606.
39 T. Higashihara, S. Fukuta, Y. Ochiai, T. Sekine, K. Chino, T. Koganezawa and I. Osaka, *ACS Appl. Polym. Mater.*, 2019, **1**, 315–320.
40 J. Choi, W. Kim, D. Kim, S. Kim, J. Chae, S. Q. Choi, F. S. Kim, T.-S. Kim and B. J. Kim, *Chem. Mater.*, 2019, **31**, 3163–3173.
41 J.-S. Kim, J.-H. Kim, W. Lee, H. Yu, H. J. Kim, I. Song, M. Shin, J. H. Oh, U. Jeong, T.-S. Kim and B. J. Kim, *Macromolecules*, 2015, **48**, 4339–4346.
42 H.-C. Hsieh, C.-C. Hung, K. Watanabe, J.-Y. Chen, Y.-C. Chiu, T. Isono, Y.-C. Chiang, R. R. Reghu, T. Satoh and W.-C. Chen, *Polym. Chem.*, 2018, **9**, 3820–3831.
43 C.-L. Liu, C.-H. Lin, C.-C. Kuo, S.-T. Lin and W.-C. Chen, *Prog. Polym. Sci.*, 2011, **36**, 603–637.
44 H. Misaka, E. Tamura, K. Makiguchi, K. Kamoshida, R. Sakai, T. Satoh and T. Kakuchi, *J. Polym. Sci., Part A: Polym. Chem.*, 2012, **50**, 1941–1952.
45 P. J. Brown, D. S. Thomas, A. Köhler, J. S. Wilson, J.-S. Kim, C. M. Ramsdale, H. Sirringhaus and R. H. Friend, *Phys. Rev. B: Condens. Matter Mater. Phys.*, 2003, **67**, 064203.
46 A. Zen, J. Pflaum, S. Hirschmann, W. Zhuang, F. Jaiser, U. Asawapirom, J. P. Rabe, U. Scherf and D. Neher, *Adv. Funct. Mater.*, 2004, **14**, 757–764.
47 F. C. Spano and C. Silva, *Annu. Rev. Phys. Chem.*, 2014, **65**, 477–500.
48 C.-C. Hung, S. Nakahira, Y.-C. Chiu, T. Isono, H.-C. Wu, K. Watanabe, Y.-C. Chiang, S. Takashima, R. Borsali, S.-H. Tung, T. Satoh and W.-C. Chen, *Macromolecules*, 2018, **51**, 4966–4975.
49 S. Savagatrup, A. S. Makaram, D. J. Burke and D. J. Lipomi, *Adv. Funct. Mater.*, 2014, **24**, 1169–1181.
50 D. Tahk, H. H. Lee and D.-Y. Khang, *Macromolecules*, 2009, **42**, 7079–7083.
51 J. T. Wang, S. Takashima, H. C. Wu, Y. C. Chiu, Y. Chen, T. Isono, T. Kakuchi, T. Satoh and W. C. Chen, *Adv. Funct. Mater.*, 2016, **26**, 2695–2705.

